

CHEMISTRY & SUSTAINABILITY

# CHEM **SUS** CHEM

ENERGY & MATERIALS

## Accepted Article

**Title:** Highly Efficient Perovskite Solar Cells Based on Zn<sub>2</sub>Ti<sub>3</sub>O<sub>8</sub> Nanoparticles as Electron Transporting Material with Efficiency over 17%

**Authors:** Zhong-Ning Chen, Aiyang Pang, Deli Shen, and Mingdeng Wei

This manuscript has been accepted after peer review and appears as an Accepted Article online prior to editing, proofing, and formal publication of the final Version of Record (VoR). This work is currently citable by using the Digital Object Identifier (DOI) given below. The VoR will be published online in Early View as soon as possible and may be different to this Accepted Article as a result of editing. Readers should obtain the VoR from the journal website shown below when it is published to ensure accuracy of information. The authors are responsible for the content of this Accepted Article.

**To be cited as:** *ChemSusChem* 10.1002/cssc.201701779

**Link to VoR:** <http://dx.doi.org/10.1002/cssc.201701779>

WILEY-VCH

[www.chemsuschem.org](http://www.chemsuschem.org)

A Journal of



# Highly Efficient Perovskite Solar Cells Based on $\text{Zn}_2\text{Ti}_3\text{O}_8$ Nanoparticles as Electron Transporting Material with Efficiency over 17%

Aiyi Pang,<sup>[a]</sup> Deli Shen,<sup>[b]</sup> Mingdeng Wei,<sup>\*[b]</sup> and Zhong-Ning Chen<sup>\*[a]</sup>

**Abstract:** Developing ternary metal oxides as electron transporting layers (ETL) for perovskite solar cell is highly challenging in the field of third-generation photovoltaics. In this study, highly mesoporous  $\text{Zn}_2\text{Ti}_3\text{O}_8$  (m-ZTO) scaffold synthesized by ion-exchange method has been successfully used as ETL for the fabrication of methyl ammonium lead halide ( $\text{CH}_3\text{NH}_3\text{PbI}_3$ ) perovskite solar cells. The optimized devices exhibit 17.21% power conversion efficiency (PCE) with open circuit voltage ( $V_{oc}$ ) of 1.02 V, short-circuit current density ( $J_{sc}$ ) of 21.97  $\text{mA cm}^{-2}$  and fill factor (FF) of 0.77 under AM 1.5 G sunlight ( $100 \text{ mW cm}^{-2}$ ). The PCE is obviously higher than that based on mesoporous ST01 (m-ST01) layer ( $\eta = 14.93\%$ ), which is ascribed to deeper conductive band of ZTO nanoparticles, better light absorption and smaller charge recombination. The devices stored for 100 days at ambient temperature with humidity of 10% show excellence stability with only 12% reduction of the PCE. The charge transmission kinetic and long-term stability parameters of the ZTO-based perovskite film growth are discussed as well.

## Introduction

Perovskite solar cells (PSCs) have recently attracted great attention due to the rapid growth of power conversion efficiency (PCE) from 3.8 % to 22.1 %.<sup>[1]</sup> As is well known, the electron transport layer (ETL) of PSCs plays an important role in extracting electrons from perovskite as well as blocking direct contact between transparent conducting oxide substrate and perovskite.<sup>[2]</sup> So far, the PSCs with PCE exceeding 20% have mainly been reported with mesoporous titanium dioxide (m- $\text{TiO}_2$ ) as an electron-transporting layer (ETL).<sup>[3]</sup> Nevertheless,  $\text{TiO}_2$ -based solar cells suffer from stability reduction under ultraviolet light, which is attributed to the changes in the compact  $\text{TiO}_2$  and/or mesoporous  $\text{TiO}_2$  layers.<sup>[4]</sup> On the other hand, ZnO as one of the most promising alternatives with a high PCE of 15.7 % was chemically unstable and prone to react with acid and

alkaline components.<sup>[5]</sup> Other binary oxides such as  $\text{SnO}_2$ ,<sup>[6]</sup>  $\text{WO}_x$ ,<sup>[7]</sup> and  $\text{In}_2\text{O}_3$ <sup>[8]</sup> have been employed as alternative ETLs in PSCs, but could not keep the long-term stability of PSCs. Compared with binary oxides, ternary oxides exhibited specific functions and highly adjustable chemical and physical properties by changing the compositions.  $\text{SrTiO}_3$  and  $\text{TiO}_2$  have similar wide band gaps, but the conduction band edge of the former is slightly higher and matches better with the band structure of  $\text{CH}_3\text{NH}_3\text{PbI}_{3-x}\text{Cl}_x$ , thus boosting  $V_{oc}$  by  $\sim 120 \text{ mV}$  and improving distinctly FF relative to mesoporous  $\text{TiO}_2$  counterparts.<sup>[9]</sup>  $\text{Zn}_2\text{SnO}_4$  ETL has a negligible effect on the transmittance of the incident light regardless of its thickness so that the thickest compact layer blocks most efficiently the back-electron transfer.<sup>[10]</sup> Noticeably, the PSCs fabricated with lanthanum doped  $\text{BaSnO}_3$  show a steady-state PCE of 21.2% and retain 93% of initial performance over 1000 hours of full-Sun illumination, which is ascribed to its high electron mobility and reasonable electronic structure.<sup>[11]</sup> As a result, there is an urgent need to explore more wide band gap ternary oxides with suitable band alignments and crystal structures to improve device performance and particularly long-term stability.

In ternary oxides study,  $\text{TiO}_2$ -ZnO systems have been explored as a new compact layers for the ETL.<sup>[12]</sup> When  $\text{TiZnO}_{12}$  (Ti : Zn : O = 1 : 1 : 12) was applied as ETL for the device, a PCE of 15.10% was achieved, which is comparable to that of the devices based on conventional  $\text{TiO}_2$  ETL. It is known that thermally stable  $\text{Zn}_2\text{Ti}_3\text{O}_8$  (ZTO) as a ternary oxide with cubic spinel type structure shows specific photocatalysis, conductivity and dielectric properties.<sup>[13]</sup> In this work, we report the first use of m-ZTO as electron transport layer in a regular mesoporous structure of  $\text{CH}_3\text{NH}_3\text{PbI}_3$  solar cells. The corresponding devices achieve PCE up to 17.21% with almost no hysteresis. Given the ZTO layer's deep conduction band and high electron mobility, the elimination of the hysteresis is ascribable to the enhanced electron extraction caused by the reduction of energy barrier at the perovskite/ETL interface. The photoluminescence (PL) quenching and transient absorption spectra show efficient photoelectron transfer from  $\text{CH}_3\text{NH}_3\text{PbI}_3$  to m-ZTO layer. Furthermore, the compact layer also blocks the electrons transporting reversely from the conducting substrate to recombine with the holes in the light-harvesting layer. By introducing such a layer into perovskite solar cell, the device efficiency is dramatically enhanced.<sup>[14]</sup>

[a] Dr. A. Y. Pang, Prof. Dr. Z. N. Chen  
State Key Laboratory of Structural Chemistry, Fujian Institute of Research on the Structure of Matter, Chinese Academy of Sciences, Fuzhou, Fujian 350002, China  
E-mail: czn@fjirsm.ac.cn

[b] Dr. D. L. Shen, Prof. Dr. M. D. Wei  
Key Laboratory of Photocatalysis on Energy and Environmental, Fuzhou University, Fuzhou, Fujian 350002, China.  
E-mail: wei-mingdeng@fzu.edu.cn

Supporting information for this article is given via a link at the end of the document.

## Results and Discussion

The X-ray diffraction (XRD) patterns in Figure 1a confirm that

ZTO synthesized by a ion-exchange method displays a cubic structural with a parameter constant  $a = 8.392 \text{ \AA}$  (JCPDS 01-087-1781).<sup>[13c]</sup> As shown in Figure 1b, the TEM images show clearly that ZTO is composed of ca. 25–45 nm size particles. The high-resolution TEM image (HRTEM) in Figure 1c shows that the nanoparticles are highly crystalline. The lattice fringes are around 0.46 and 0.59 nm, respectively, corresponding to  $d(111)$  and  $d(110)$ -spacing in the XRD patterns. Moreover, the ring-like selected area electron diffraction (SAED; the inset in Figure 1d) pattern indicates that the as-prepared ZTO nanoparticles exhibit polycrystalline nature. The stoichiometry of ZTO has also been confirmed by TEM-mapping measurement (Figure S1) and XPS (Figure S2).

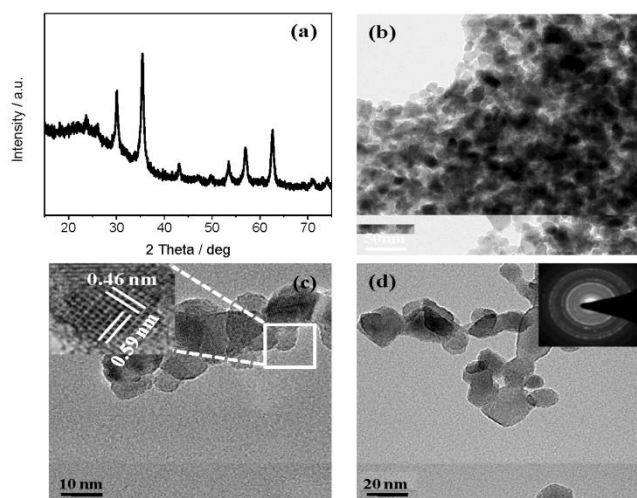


**Figure 1.** XRD pattern (a), TEM image (b), HRTEM image (c) and SAED image (d) of ZTO nanoparticles obtained at calcined temperatures 600 °C.

We fabricated  $\text{CH}_3\text{NH}_3\text{PbI}_3$  films on FTO/c-TiO<sub>2</sub> (abbreviated as c-TO)/m-ZTO substrate through a one-step procedure according to the literature.<sup>[15]</sup> The film quality of the perovskite is shown in Figure 2. The corresponding XRD patterns of the as-prepared  $\text{CH}_3\text{NH}_3\text{PbI}_3$  films based on m-ZTO substrate are depicted in Figure 2a. A set of diffraction peaks occurring at 14.08, 28.41, 31.85, and 43.19° arise from an orthorhombic crystal structure of  $\text{CH}_3\text{NH}_3\text{PbI}_3$  crystals, which are assigned to (110), (220), (310) and (330) crystal faces, respectively.<sup>[16]</sup> The absence of the peak of 12.65° is indicative of a complete consumption of  $\text{PbI}_2$  in the perovskite films based on m-ZTO.<sup>[17]</sup> The as-formed perovskite films on m-ZTO substrates (Figure 2b) display the characteristics of uniformity, free pinhole porosity and low grain boundary with densely microscale packed grains, thus implying its promising advantages for PSC devices. The surface roughness of the perovskite film on m-ZTO is very small ( $R_q = 8.91 \text{ nm}$ ), as revealed by AFM measurement in Fig 2c. Furthermore, the typical cross-sectional SEM image (Figure 2d) of the device displays its mesoporous architecture. The thickness of each layer is estimated to be ca. 70 nm for the compact c-TO, ca. 350

nm for the  $\text{CH}_3\text{NH}_3\text{PbI}_3$  layer combined with mesoporous m-ZTO, ca.180 nm for the hole-transporting layer, and 80 nm for the back contact of thermally evaporated Au layer. It is also clearly shown that the intimate contact was well achieved between  $\text{CH}_3\text{NH}_3\text{PbI}_3$  and adjacent layers in our devices.

For the purpose of comparison, perovskite film on the m-STO1 substrate was also investigated as shown in Figure S3. Both ETLs of m-ZTO and m-STO1 had almost no effect on the perovskite morphology in SEM, but a higher peak (12.65°) in XRD, a higher roughness ( $R_q = 12.7 \text{ nm}$ ) in AFM and a thinner thickness (~310 nm) of  $\text{CH}_3\text{NH}_3\text{PbI}_3$  layer were observed indeed. This is attributed to a coarser surface, a worse wettability and a lower infiltrating of m-STO1. As indicated in in Figure S4, m-ZTO film ( $R_q = 27.8 \text{ nm}$ ) shows a more uniform and dense surface than that of m-STO1 film ( $R_q = 36.7 \text{ nm}$ ) which has an irregular surface with some obvious valleys. The much smaller contact angle of DMSO droplet on m-ZTO film (3.4°) than that on m-STO1 (28.3°) owing to a good wettability of the former (Figure S4) is beneficial for perovskite solution to infiltrate into m-ZTO and crystallize into a stronger and thicker light-absorbing layer.

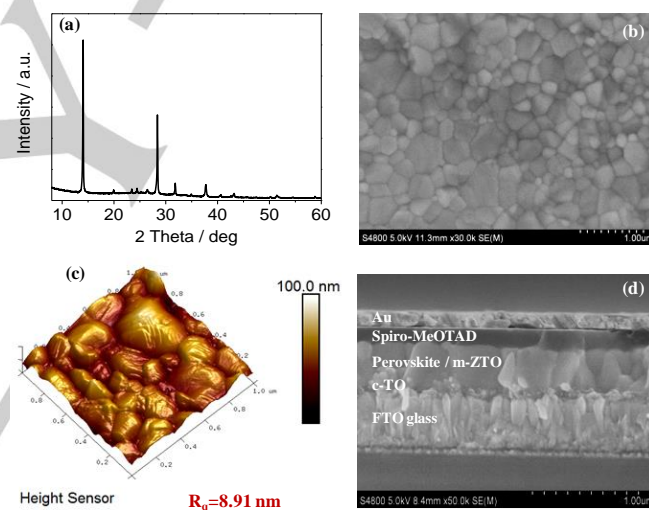


**Figure 2.** Perovskite film on the FTO/c-TO/m-ZTO substrate. (a) XRD pattern. (b) Top-view SEM image, scale bar 1 µm. (c) 3D AFM topography image (1.0x1.0 µm). (d) The cross-sectional SEM image of the device.

The current density–voltage (J–V) curves and incident photon-to-current efficiency (IPCE) spectra are shown in Figure 3 for the champion mesoporous PSCs based on m-ZTO and m-STO1 ETLs, and its photovoltaic characteristic are summarized in Table 1. Moreover, to optimize the photovoltaic performance of PSCs based on ZTO ETLs, the thickness of the m-ZTO film was optimized through repeatedly spin-coating process (Figure S5 and Table S1). To obtain superior efficiency, the optimum thickness for the m-ZTO ETL prepared by spin-coating for two times was ca. 200 nm. Although the devices based on m-ZTO and m-STO1 exhibited comparable  $V_{oc}$  values of 1.02 and 0.99 V, respectively, the corresponding  $J_{sc}$  and FF values were different

as shown in Figure 3a. The cells based on m-ZTO ( $J_{sc} = 21.97$  mA cm<sup>-2</sup> and PCE = 17.21%) exhibited distinctly higher  $J_{sc}$  and PCE than those of m-ST01-based cells ( $J_{sc} = 20.48$  mA cm<sup>-2</sup> and PCE = 14.93%). The large efficiency enhancement of m-ZTO based PSCs compared with that of m-ST01 based devices is likely attributed to the higher light absorption and the increased charge carrier concentration for the former. The low dark current (J-V in Figure 3a and J-V in log scales in Figure S6) arises most likely from the high-quality films, which may induce to decrease recombination when carriers are separated in the light absorbing layer. The improvement of FF is mostly attributable to the decrease of leakage currents and the less series resistance of the m-ZTO based CH<sub>3</sub>NH<sub>3</sub>PbI<sub>3</sub> films with large grains and few boundaries over a range of length scale,<sup>[18]</sup> which is consistent with the following resistance measurements.

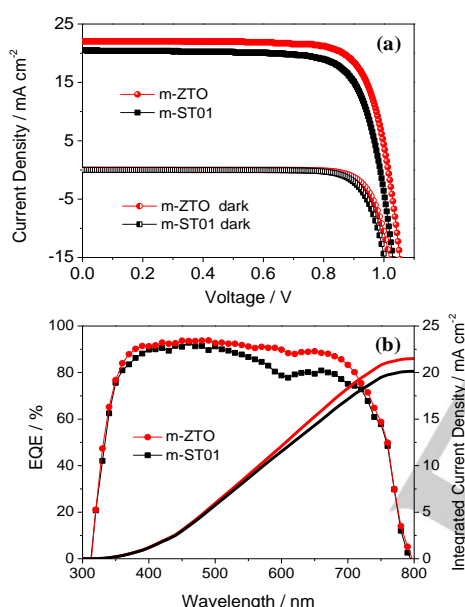


**Figure 3** (a) J-V curves and (b) IPCE spectra and the integrated photocurrent of the solar cells based on the as-prepared perovskite films under AM 1.5G illumination.

**Table 1.** Summary of photovoltaic performances metrics of the champion devices fabricated on m-ZTO and m-ST01.

Sample	$J_{sc}$ /mA cm <sup>-2</sup>	$V_{oc}$ /V	FF / %	$\eta$ / %
m-ZTO <sub>max</sub>	21.97	1.02	76.57	17.21
m-ST01 <sub>max</sub>	20.48	0.99	73.69	14.93

Figure 3b shows the IPCE spectra of the best performance devices. Photocurrent generation starts at 780 nm in agreement with the band gap of the CH<sub>3</sub>NH<sub>3</sub>PbI<sub>3</sub> and achieves peak values of ~90% in the 380–680 nm spectral region.<sup>[19]</sup> By integrating the density photocurrents of the IPCE spectrum, m-ZTO based

PSCs achieved a larger current density (21.36 mA/cm<sup>2</sup>) than that of m-ST01 (19.86 mA/cm<sup>2</sup>) based devices under the AM 1.5G solar photon flux. Relative to  $J_{sc}$  from J-V measurement, the total photocurrent collected from IPCE spectrum is slightly lower, due probably to the surface charge traps of ETLs.<sup>10</sup> A contributing factor to the effective PCE is the high electron injection power between the absorber film and m-ZTO. More thorough and objective study is under way to get more insight to the relationship between the film property and the device performance.

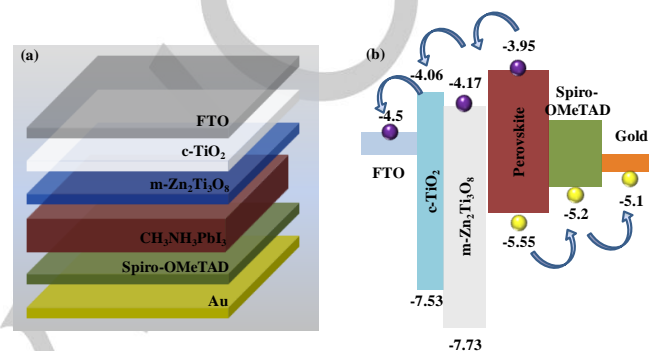


**Figure 4.** Schematic diagrams of the device structure (a) and the energy level of the mesoporous perovskite solar cell (b).

The PSC architecture is FTO/c-TiO<sub>2</sub>/m-ZTO/CH<sub>3</sub>NH<sub>3</sub>PbI<sub>3</sub>/Spiro-OMeTAD/Au as schematically illustrated in Figure 4a. To obtain a clear understanding of the electron transfer pathway through the ETLs, an energy band diagram was drawn based on the appropriate band levels (Figure S7 and Table S2). Figure 4 demonstrates that both the conduction band minima (CBM) and valence band maxima (VBM) are shifted in a downward direction upon using ternary oxide ZTO with respect to c-TiO<sub>2</sub>. This downward shift in the CBM position correspond well with the perovskite energy band level, which facilitates electron injection and thus improves  $J_{sc}$  from 20.48 (m-ST01) to 21.97 (m-ZTO) mA cm<sup>-2</sup>.<sup>[18]</sup> Just like semiconductor of binary oxide, ZTO exists sites in the tail of the density states to move the quasi-Fermi level in the material nearly to the bottom of conduction band under illumination.<sup>[20]</sup> The higher  $V_{oc}$  and FF indicate that fewer surface and sub-band gap states are exhibited in the mesoporous ZTO than those in ST01. According to a recent study, the downward shift of ZTO VBM position results in hole blocking and less recombination in the interface at the m-ZTO/electrode interface.<sup>[21]</sup> The TO layer between ZTO and FTO exhibits a higher CBM than that of both ZTO and FTO, which benefits to retard charge-carrier recombination at the interfaces. It is speculated that higher CBM of c-TiO<sub>2</sub> does not hinder the flow of charges because the energy level of the lowest unoccupied molecular orbital of the CH<sub>3</sub>NH<sub>3</sub>PbI<sub>3</sub> layer is higher than the CBM of ZTO and c-TiO<sub>2</sub>. Thus, efficient charge extraction is valid in our cells as that found in other similar structure devices.<sup>[22]</sup>

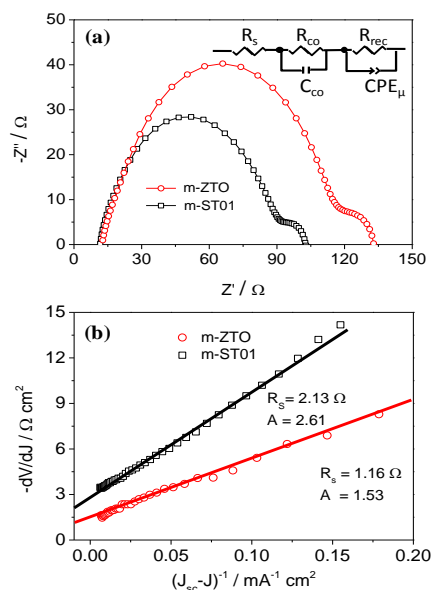


**Figure 5.** (a) EIS and (b) plots of  $dV/dJ$  vs  $(J_{sc} - J)^{-1}$  derived from I-V curves (Figure 3a) of m-ST01 (black) and m-ZTO (red) based cells.

Electrochemical impedance spectroscopy (EIS) is a simple but useful method to investigate the charge recombination resistance and interfacial properties of perovskite solar cells. As shown in Figure 5, Nyquist plots of the devices under dark at an applied bias voltage of 0.7 V with the frequency range of 0.1 to 100 kHz display two distinct semicircles. The Nyquist plots were fitted using an equivalent circuit model as illustrated in the inset of Figure 5. The curve fitting data of both the ST01 and ZTO ETL-based devices are summarized in Table 2. The series of resistance ( $R_s$ ) is associated with the wiring and FTO substrate located in the high-frequency region. The  $R_{co}$  and  $C_{co}$  refer to the interface resistance of the counter electrode and the corresponding capacitance, respectively. In the Nyquist plots, the main arc is responsible for a combination of the recombination resistance ( $R_{rec}$ ) and the chemical capacitance (CPE) in the ETLs/ $\text{CH}_3\text{NH}_3\text{PbI}_3$ /spiro-OMeTAD interfaces.<sup>[23]</sup> Figure 5a shows that the  $R_{co}$  and  $R_s$  of the our both cells approached to each other because the same counter electrodes and measurement methods are applied. However, compared with that in m-ST01-based interfaces ( $336.2 \Omega\cdot\text{cm}^2$ ), the  $R_{rec}$  of ZTO-based interfaces is increased to  $486.7 \Omega\cdot\text{cm}^2$ . The increased  $R_{rec}$  (inversely related to the interface recombination rate) indicates that electron back flow from the ZTO to spiro-OMeTAD is retarded and the charge transfer resistance at the interfaces c-TO/m-ZTO/ $\text{CH}_3\text{NH}_3\text{PbI}_3$  increased. This is in agreement with the measurement of dark current curves. Moreover, agreeing with the impedance measurement, the series of resistance of the m-ZTO based cells ( $1.16 \Omega$ ) exhibits an obvious decrease compared with that of m-ST01 based one ( $2.13 \Omega$ ), as shown in Figure 5b.<sup>[24]</sup> In a solar cell, a lower  $R_s$  is necessary to decrease current leakage at high bias voltages so that the FF and  $V_{oc}$  were increased by about 3.9% and 3.0%

(Table 1), respectively. Finally, the PCE is enhanced from 14.93% to 17.21% when ZTO is substituted for commercially purchased ST01.

**Table 2.** Deconvoluted resistances from impedance analyses for m-ZTO and m-ST01 ETLs.

ETL	$R_s / \Omega\cdot\text{cm}^2$	$R_{co} / \Omega\cdot\text{cm}^2$	$R_{rec} / \Omega\cdot\text{cm}^2$
m-ZTO	2.5	92.8	486.7
m-ST01	4.2	87.8	336.2

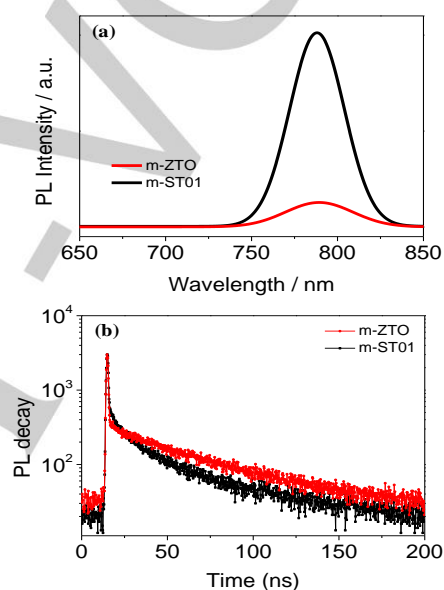


**Figure 6.** The steady-state PL spectra (a) and time-resolved PL (TRPL) decay curves (b) of  $\text{CH}_3\text{NH}_3\text{PbI}_3$  deposited on the top of m-ZTO and m-ST01.

To investigate the charge injection/separation behavior, we measured steady-state photoluminescence (PL) spectra and time-resolved PL (TRPL) decay curves of FTO/c-TO/m-ZTO/ $\text{CH}_3\text{NH}_3\text{PbI}_3$  and FTO/c-TO/m-ST01/ $\text{CH}_3\text{NH}_3\text{PbI}_3$  films. Figure 6a shows that the spectral band centered at 766 nm related to the intrinsic fluorescence emission of  $\text{CH}_3\text{NH}_3\text{PbI}_3$  was quenched by contact with the ETLs, indicating that electron transfer from the perovskite to the ETLs is indeed operating. Compared with that of m-ST01/perovskite, the PL intensity of m-ZTO/perovskite is obviously lower, indicating that the charge extraction from the perovskite is more efficient for ZTO ETL. The fast decay corresponds to the quenching of carriers from the perovskite to the ETLs and the slow decay is considered to be the result of radiative decay within the perovskite film as shown in Figure 6b and Table S3.<sup>[25]</sup> The PL quenching in the FTO/c-TO/m-ZTO/ $\text{CH}_3\text{NH}_3\text{PbI}_3$  film was faster than that in the FTO/c-TO/m-ST01/ $\text{CH}_3\text{NH}_3\text{PbI}_3$  film, implying the high speed transformation of the charge carriers from light-harvesting layer to the former ETL. From the deconvolution algorithm of TRPL

decay curves with bi-exponential function, it is found that the fast PL lifetime of FTO/c-TO/m-ZTO/CH<sub>3</sub>NH<sub>3</sub>PbI<sub>3</sub>/spiro-OMeTAD/Au mesoporous hybrid solar cell ( $\tau_1=1.27$  ns) is obviously shorter than that of the traditional FTO/c-TO/m-STO1/CH<sub>3</sub>NH<sub>3</sub>PbI<sub>3</sub>/spiro-OMeTAD/Au mesoporous hybrid solar cell ( $\tau_1=2.12$  ns). Moreover, the slow decay feature based on ZTO shows a higher time coefficient ( $\tau_2=167.4$  ns) than that of ST01 ( $\tau_2=97.6$  ns) so as to retard recombination and enhance PV performance. This suggests that the charge injection from CH<sub>3</sub>NH<sub>3</sub>PbI<sub>3</sub> to m-ZTO is more impactful than that to m-STO1 and accordingly the charge injection/separation efficiency is advanced in the FTO/c-TO/m-ZTO/CH<sub>3</sub>NH<sub>3</sub>PbI<sub>3</sub>/spiro-OMeTAD/Au mesoporous perovskite hybrid solar cells.

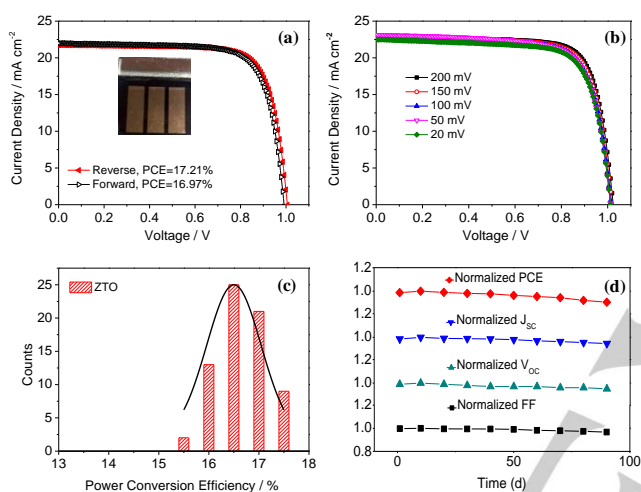


**Figure 7.** (a) J–V curves for hysteresis tests (open and closed circles stand for forward and reverse scans, respectively). (b) J–V curves at various scan rates in reverse scan conditions for the same device. (c) Statistical histogram of PCE for 70 measured devices, fitted with a Gaussian distribution (black line). (d) Long-term stability test of the inverted perovskite solar cells stored at room temperature with humidity of 10%.

Owing to the charge traps and interface defects of the low quality perovskite film, the photocurrent hysteresis behavior is another critical issue in perovskite solar cells.<sup>[26]</sup> As depicted in Figure 7a, the hysteresis was almost unobserved at 20  $\text{mV s}^{-1}$  scan rate in the J–V curves of m-ZTO cells, where PCE = 17.21% for the reverse direction and 16.97% for the forward direction. The J–V curves with variable scan rates ranging from 20 to 200  $\text{mV s}^{-1}$  further reveal that photocurrents hysteresis are almost independent on the scan-rates (Figure 7b and Table S4). As a result, the prepared perovskite films based on m-ZTO ETLs had excellent characteristics, in which the defects and grain boundary were mostly eliminated and the charge transfer highly enhanced.<sup>[27]</sup> As depicted in Figure 7c and Table S5, the PCE statistics from 70 cells exhibit a normal distribution with a small discreteness and a good central tendency. On average, a 3–4% increase in absolute PCE is observed by the use of m-ZTO with the larger grain sizes in perovskite films. Significantly, the high-

efficiency devices reported herein show good repeatability and long-term stability when stored in the air under room temperature with humidity of 10% as illustrated in Figure 7d. We tested the stability of 20 devices under illumination with AM 1.5 G (100  $\text{mW cm}^{-2}$ ) light in air. The PCE decreases slowly ca. 12% in 100 days at humidity of 10%. Therefore, the photovoltaic data of 20 devices suggest that the devices based on m-ZTO are repeatable and stable in a long term.

## Conclusions

We have successfully demonstrated that wideband-gap ZTO can be effectively employed as a mesoporous layer between c-TO and perovskite absorber layer to obtain high-performance PSCs. A simple spin-coated ZTO scaffold inserted onto c-TO results in a downward shift in conduction band energy level and the suppression of interfacial charge recombination so as to improve dramatically electron injection efficiency in perovskite solar cells. An obvious increased PCE for ZTO ETL (17.21%) with good reproducibility was achieved relative to that for m-STO1-based counterpart (14.93%). The EIS and TRPL analyses reveal that ZTO ETL has a decreased charge recombination and thus contributes to the improvement of the  $V_{oc}$  and FF. The XPS analysis confirms a negative shift in the conductive band potential of ZTO, thus facilitating fast and easy electron transfer from highly mobile CH<sub>3</sub>NH<sub>3</sub>PbI<sub>3</sub> to the conduction band of ZTO. The devices display only 12% decrease of the PCE after 100 days at ambient temperature and 10% humidity with excellent stability. Our findings demonstrate that the use of ternary oxide is a promising approach to tune  $E_g$  and thereby reduce interface charge recombination in the perovskite solar cells.

## Experimental Section

**Materials** All chemicals and reagents were used as received without any further purification. Methylamine (33 wt. % in absolute ethanol), hydrochloric acid (37%), lead iodide (PbI<sub>2</sub>, 99.9%), 2-propanol (99.7%), dimethyl sulfoxide (DMSO, 99.9%) and chlorobenzene (99.8%) were purchased from Sigma–Aldrich. 2,2',7,7'-Tetrakis(N,N-di-p-methoxyphenylamine)-9,9'-spirobifluorene (spiro-OMeTAD) was obtained from Borun Chemical (98%, Ningbo, China).

**ZTO Preparation** The ZTO nanoparticles were synthesized using titanate Na<sub>x</sub>H<sub>2-x</sub>Ti<sub>3</sub>O<sub>7</sub> nanotubes as a precursor.<sup>[28]</sup> In a typical synthetic procedure, 1 g of TiO<sub>2</sub> powder (ST01, 10 nm, Ishihara Sangyo Kaisha, Ltd., Japan) and an aqueous solution of NaOH (10 M, 200 mL) were placed into a Teflon container. The mixture was vigorously stirred in an oil bath at 120 °C for 20 h. The white suspension of titanate nanotubes was filtrated and washed with 1 M dilute HCl and then deionized water until a pH  $\approx$  7 was obtained. Then, an aqueous ammonia solution was slowly added to an aqueous solution of ZnCl<sub>2</sub>·6H<sub>2</sub>O. After a clear solution formed, the precursor titanate nanotubes were dispersed into this solution with stirring at 60 °C for 1 d. Finally, the products were carefully washed with deionized water for several times, dried and calcined at 600 °C for 3 h in air.

**CH<sub>3</sub>NH<sub>3</sub>I Synthesis** The CH<sub>3</sub>NH<sub>3</sub>I was synthesized and purified by the procedures described in literature.<sup>[29]</sup> To a methanol (33 wt. %, 24 mL) solution of methylamine was slowly added hydroiodic acid (57 wt%, 10 mL) at 0 °C. After stirring under a N<sub>2</sub> atmosphere for 2 h, the mixture was evaporated at 50 °C for 1 h to remove volatile substances. The as-obtained product was washed with absolute diethyl ether for three times and then dried at 60 °C in a vacuum oven for 12 h to afford the desired CH<sub>3</sub>NH<sub>3</sub>I as white crystals.

**Device fabrication.** The ZTO and ST01 pastes were prepared by our previously described procedures.<sup>[22]</sup> Substrate preparation was carried out under ambient conditions. Firstly, FTO-coated glass (13 Ω/sq, Aldrich) was patterned by etching with Zn powder and 2 M HCl. Secondly, the substrates were cleaned with detergent (diluted to the volume ratio of 15% with deionized water), rinsed with deionized water, acetone and isopropyl alcohol, and then dried with clean dry air. After oxygen treatment, the clean substrates were spin-coated with 0.15 M titanium diisopropoxide bis(acetylacetonate) at 2,000 r.p.m. for 30 s. After drying at 120 °C for 15 min, the same spin-coating and annealing process was used for the mesoporous electron transportation layer with the mere difference by replacing TiO<sub>2</sub> nanocolloidal solution with the homemade ZTO nanoparticle paste (dilute with ethanol, v/v 1:6), which was performed repeatedly in order to increase film thickness. The films were sintered again at 500 °C for 30 min. Upon cooling to room temperature, m-ZTO were infiltrated with the perovskite precursor solution in a nitrogen-filled glovebox, which was prepared by dissolving a stoichiometric amount (1:1 molar ratio) of lead iodide and methyl ammonium iodide in DMSO at a concentration of 1.2 M of each component.<sup>[15]</sup> The spin coating procedures include two steps, that is, at 6000 rpm first for 20 s and then 10 s by gently dropping chlorobenzene on the spinning substrate through a micro pipette. The substrate was then heated at 100 °C for 1 h on a hot plate in the nitrogen-filled glovebox. Upon drying, 60 μL of spiro-OMeTAD solution was spin-coated on the CH<sub>3</sub>NH<sub>3</sub>PbI<sub>3</sub> layer at 3000 rpm for 20 s. The solution was prepared by dissolving 72 mg of spiro-OMeTAD in 1 mL of chlorobenzene, to which 28.8 μL of 4-tert-butyl pyridine and 14.4 μL of lithium bis(trifluoromethanesulfonyl)imide (Li-TFSI) solution (520 mg Li-TFSI in 1 mL of acetonitrile) were added. Finally, 80 nm of gold was deposited at ~10<sup>-6</sup> bar via thermal evaporation on the spiro-OMeTAD coated film.

**Characterization** The X-ray diffraction (XRD) patterns were recorded on a PANalytical X'Pert spectrometer using Co Kα radiation (λ = 1.78897 Å) and the data were converted to Cu Kα data. The scanning electron microscopy (SEM) was measured on a Hitachi S4800 instrument. The transmission electron microscopy (TEM) and selected area electron diffraction (SAED) pattern images were recorded on a Tecnai G2 F20 (FEI) with an accelerated photovoltage of 200 kV. N<sub>2</sub> adsorption-desorption analysis was carried on a Micromeritics ASAP 2020 instrument. The UV-vis spectra were measured on Lambda-9 (Perkin-Elmer) spectrometer. The atomic force microscopy (AFM) was used to characterize the texture and roughness of films on a Dimension ICON, Bruker. The steady-state photoluminescence (PL) and time-resolved PL spectroscopy of CH<sub>3</sub>NH<sub>3</sub>PbI<sub>3</sub> coated on both the m-ZTO and m-ST01 ETLs were performed using Edinburgh FLS920 instrument with picosecond pulsed diode laser of 375 nm. The ultraviolet photoelectron spectroscopy (UPS) for both m-ZTO and c-TO were measured using ESCALAB 250Xi (Thermo Fisher) under a background pressure of 5.0 × 10<sup>-7</sup> Pa.

The photovoltaic performance in terms of J-V characteristics was determined using a solar simulator (Sol3A Class AAA, Oriel Instruments, Stratford, CT, USA) and a Keithley 2440 source measurement unit (Keithley Instruments Inc., Cleveland, OH, USA) under air mass (AM) 1.5

and 1 sun (100 mW cm<sup>-2</sup>) conditions. The 1 sun light intensity level was calibrated using a standard Si reference cell certified by the Newport Corporation. All the devices were measured in a light tight sample holder with an active area of 0.12 cm<sup>2</sup> for each cell and fixed using an aperture mask. The IPCE was recorded using a quantum efficiency measurement system (QEX10, PV Measurements, Inc.) in the wavelength range from 300 to 850 nm. The EIS was obtained using a potentiostat (IM-6, Zahner) in the frequency range from 0.1 to 100 kHz, applying the V<sub>oc</sub> derived from the J-V test and under dark conditions.

## Acknowledgements

This work was financially supported by National Natural Science Foundation of China (21603230 and 91433104), the 973 project from MSTC (2014CB845603), the CAS/SAFEA International Partnership Program for Creative Research Teams, and the Strategic Priority Research Program of the Chinese Academy of Sciences (XDB20000000).

**Keywords:** charge transmission, electron transport layer, perovskite solar cell, ternary metal oxide, zinc titanate oxide

- [1] a) A. Kojima, K. Teshima, Y. Shirai, T. Miyasaka, *J. Am. Chem. Soc.* **2009**, *131*, 6050-6051; b) H. R. Tan, A. Jain, O. Voznyy, X. Z. Lan, F. P. G. d. Arquer, J. Z. Fan, R. Q. Bermudez, M. J. Yuan, B. Zhang, Y. C. Zhao, F. J. Fan, P. C. Li, L. N. Quan, Y. B. Zhao, Z. H. Lu, Z. Y. Yang, S. Hoogland, E. H. Sargent, **2017**, *355*, 722-726.
- [2] a) T. Salim, S. Sun, Y. Abe, A. Krishna, A.C. Grimsdale, Y.M. Lam, *J. Mater. Chem. A* **2015**, *3*, 8943-8969; b) A. Marchioro, J. Teuscher, D. Friedrich, M. Kunst, R.V.D. Kril, T. Moehl, M. Grätzel, J.E. Moser, *Nat. photon.* **2014**, *8*, 250-255; c) P.P. Boix, K. Nomura, N. Mathews, S.G. Mhaisalkar, *Mater. Today* **2014**, *17*, 16-23.
- [3] a) J. Burschka, N. Pellet, S.J. Moon, R.H. Baker, P. Gao, M.K. Nazeeruddin, M. Grätzel, *Nature* **2013**, *499*, 316-319; b) H. P. Zhou, Q. Chen, G. Li, S. Luo, T. Song, H.S. Duan, Z.R. Hong, J.B. You, Y.S. Liu, Y. Yang, *Science* **2014**, *345*, 542-546; c) M. Saiiba, S. Orlandi, T. Matsui, S. Aghazada, M. Cavazzini, J.P. Correa-Baena, P. Gao, R. Scopelliti, E. Mosconi, K.H. Dahmen, F.D. Angelis, A. Abate, A. Hagfeldt, G. Pozzi, M. Grätzel, M.K. Nazeeruddin, *Nature Energy* **2016**, *1*, 15017.
- [4] a) T. Leijtens, G.E. Eperon, S. Pathak, A. Abate, M.M. Lee, H.J. Snaith, *Nat. Commun.* **2013**, *4*, 2885; b) W. Li, W. Zhang, S.V. Reenen, R.J. Sutton, J. Fan, A.A. Haghighirad, M.B. Johnston, L. Wang, H.J. Snaith, *Energy Environ. Sci.* **2016**, *9*, 490-498.
- [5] D. Liu, T.L. Kelly, *Nat. Photonics* **2013**, *8*, 133-138.
- [6] a) W.J. Ke, G. Fang, J.Q. Liu, L.B. Xiong, P.L. Qin, H. Tao, J. Wang, H.W. Lei, B.R. Li, J.W. Wan, G. Yang, Y.F. Yan, *J. Am. Chem. Soc.* **2015**, *137*, 6730-6733; b) H.S. Rao, X.B. Chen, W.G. Li, Y.F. Xu, H.Y. Chen, D.B. Kuang, C.Y. Su, *Adv. Funct. Mater.* **2015**, *25*, 7200-7207.
- [7] K. Wang, Y. Shi, Q. Dong, Y. Li, S. Wang, X. Yu, M. Wu, T. Ma, *J. Phys. Chem. Lett.* **2015**, *6*, 755-759.
- [8] M. Qin, J. Ma, W. Ke, P. Qin, H. Lei, H. Tao, X. Zheng, L. Xiong, Q. Liu, Z. Chen, J. Lu, G. Yang, G. Fang, *ACS Appl. Mater. Interfaces* **2016**, *8*, 8460-8466.
- [9] A. Bera, K. Wu, A. Sheikh, E. Alarousu, O.F. Mohammed, T. Wu, *J. Phys. Chem. C* **2014**, *118*, 28494-28501.
- [10] S.S. Mali, C.S. Shim, C.K. Hong, *Sci. Rep.* **2015**, *5*, 11424.
- [11] S.S. Shin, E.J. Yeom, W.S. Yang, S. Hur, M.G. Kim, J. Im, J. Seo, J.H. Noh, S.I. Seok, *Science* **2017**, *356*, 167-171.

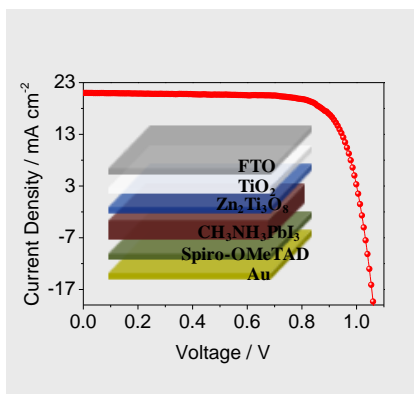
- [12] X. Yin, Z.Z. Xu, Y.J. Guo, P. Xu, M. He, *ACS Appl. Mater. Interfaces* **2016**, *8*, 29580-29587.
- [13] a) Z.T. Zhang, A.J. Rondinone, J.X. Ma, J. Shen, S. Dai, *Adv. Mater.* **2005**, *17*, 1415-1419; b) M. Zhao, B.P. Bastakoti, Y.Q. Li, H. Xu, J.H. Ye, Z.W. Liu, Y. Yamauchi, *Chem. Commun.* **2015**, *51*, 14582-14585; c) Z.S. Hong, M.D. Wei, Q.X. Deng, X.K. Ding, L.L. Jiang, K.M. Wei, *Chem. Commun.* **2010**, *46*, 740-742; d) Y.L. Huang, D.C. Tsai, Y.C. Lee, D.R. Jung, F.S. Shieu, *Surf. Coat. Tech.* **2013**, *231*, 153-156.
- [14] E.J. Juarez-Perez, M. Wussler, F. Fabregat-Santiago, K. LakusWollny, E. Mankel, T. Mayer, W. Jaegermann, Mora-Sero I., *J. Phys. Chem. Lett.* **2014**, *5*, 680-685.
- [15] A. Abate, S. Paek, F. Giordano, J. Correa-Baena, M. Saliba, P. Gao, T. Matsui, J. Ko, S.M. Zakeeruddin, K.H. Dahmen, A. Hagfeldt, M. Grätzel, M.K. Nazeeruddin, *Energy Environ. Sci.* **2015**, *8*, 2946-2953.
- [16] M. Liu, M.B. Johnston, H.J. Snaith, *Nature* **2013**, *501*, 395-398.
- [17] J.Y. Jeng, K.C. Chen, T.Y. Chiang, P.Y. Lin, T.D. Tsai, Y.C. Chang, T.F. Guo, P. Chen, T.C. Wen, Y.J. Hsu, *Adv Mater.* **2014**, *26*, 4107-4113.
- [18] Q. Chen, H.P. Zhou, Z.Z. Hong, S. Luo, H.S. Duan, H.H. Wang, Y.S. Liu, G. Li, Y. Yang, *J. Am. Chem. Soc.* **2014**, *136*, 622-625.
- [19] I. Jeong, H. Jung, M. Park, J.S. Park, H.J. Son, J. Joo, J. Lee, M.J. Ko, *Nano Energy* **2016**, *28*, 380-389.
- [20] M.L. Michael, J. Teuscher, T. Miyasaka, T.N. Murakami, H. J. Snaith, *Science* **2012**, *338*, 643-647.
- [21] a) C. Huang, C. Liu, Y. Di, W. Li, F. Liu, L. Jiang, J. Li, X. Hao and H. Huang, *ACS Appl. Mater. Interfaces* **2016**, *8*, 8520-8526; b) S.F. Shaikh, H.C. Kwon, W. Yang, H. Hwang, H. Lee, E. Lee, S. Ma, J. Moon, *J. Mater. Chem. A* **2016**, *4*, 15478-15485.
- [22] A.Y. Pang, X. Sun, H.C. Ruan, Y.F. Li, S.Y. Dai, M.D. Wei, *Nano Energy* **2014**, *5*, 82-90.
- [23] H. Kim, K.G. Lim, T.W. Lee, *Energy Environ. Sci.* **2016**, *9*, 12-30.
- [24] H.Y. Zhang, J.J. Shi, X. Xu, L.F. Zhu, Y.H. Luo, D.M. Li, Q.B. Meng, *J. Mater. Chem. A* **2016**, *4*, 15383-15389.
- [25] a) G. Niu, W. Li, F. Meng, L. Wang, H. Dong, Y. Qiu, *J. Mater. Chem. A* **2014**, *2*, 705-710; b) B. Duan, Y.K. Ren, Y.F. Xu, W.Y. Chen, Q. Ye, Y. Huang, J. Zhu, S.Y. Dai, *Inorg. Chem. Front.* **2017**, *4*, 473-480; c) X.M. Wen, R. Sheng, A.W.Y. Ho-Baillie, A. Benda, S.H. Woo, Q.S. Ma, S.J. Huang, M.A. Green, *J. Phys. Chem. Lett.* **2014**, *5*, 3849-3853.
- [26] a) I.C. Smith, E.T. Hoke, D. Solis-Ibarra, M.D. McGehee, H.I. Karunadasa, *Angew. Chem. Int. Ed.* **2014**, *53*, 11232-11235; b) D.H. Cao, C.C. Stoumpos, O.K. Farha, J.T. Hupp, M.G. Kanatzidis, *J. Am. Chem. Soc.* **2015**, *137*, 7843-7850.
- [27] C.G. Wu, C.H. Chiang, Z.L. Tseng, M.K. Nazeeruddin, A. Hagfeldt, M. Grätzel, *Energy Environ. Sci.* **2015**, *8*, 2725-2733.
- [28] a) Y. Yang, X.W. Sun, B.K. Tay, J.X. Wang, Z.L. Dong, H.M. Fan, *Adv. Mater.* **2007**, *19*, 1839-1844; b) Y. Yang, R. Scholz, H.J. Fan, D. Hesse, U. Gösele, M. Zacharias, *ACS Nano* **2009**, *3*, 555-562.
- [29] J.H. Im, C.R. Lee, J.W. Lee, S.W. Park, N.G. Park, *Nanoscale* **2011**, *3*, 4088-4093.

Entry for the Table of Contents (Please choose one layout)

Layout 1:

## FULL PAPER

Ternary metal oxide zinc titanate oxide ( $Zn_2Ti_3O_8$ ) is first used as a mesoporous electron transporting layer in perovskite solar cells to achieve the highest photoconversion efficiency of 17.21%. The efficiency decreases ca. 12% in the 100 days with good reproducibility and stability in long term.



Aiyang Pang,<sup>[a]</sup> Deli Shen,<sup>[b]</sup> Mingdeng Wei,<sup>[b]</sup> and Zhong-Ning Chen<sup>[a]</sup>

Page No.1 – Page No.7

Highly Efficient Perovskite Solar Cells Based on  $Zn_2Ti_3O_8$  Nanoparticles as Electron Transporting Material with Efficiency over 17%